

# Non-invasive measurement of X-ray beam heating on a surrogate crystal sample

Edward H. Snell,<sup>a\*</sup> Henry D. Bellamy,<sup>b</sup> Gerd Rosenbaum<sup>c</sup> and Mark J. van der Woerd<sup>d</sup>

<sup>a</sup>Hauptman Woodward Medical Research Institute, 700 Elicott Street, Buffalo, NY 14203, USA,

<sup>b</sup>CAMD, Louisiana State University, 6980 Jefferson Highway, Baton Rouge, LA 70806, USA,

<sup>c</sup>Department of Biochemistry, University of Georgia, SERCAT at APS, Argonne, IL 60439, USA, and

<sup>d</sup>Department of Biochemistry and Molecular Biology, Colorado State University, Fort Collins, CO 80523, USA. E-mail: esnell@hwi.buffalo.edu

Cryocooling is a technique routinely used to mitigate the effects of secondary radiation damage on macromolecules during X-ray data collection. Energy from the X-ray beam absorbed by the sample raises the temperature of the sample. How large is the temperature increase and does this reduce the effectiveness of cryocooling? Sample heating by the X-ray beam has been measured non-invasively for the first time by means of thermal imaging. Specifically, the temperature rise of 1 mm and 2 mm glass spheres (sample surrogates) exposed to an intense synchrotron X-ray beam and cooled in a laminar flow of nitrogen gas is experimentally measured. For the typical sample sizes, photon energies, fluxes, flux densities and exposure times used for macromolecular crystallographic data collection at third-generation synchrotron radiation sources and with the sample accurately centered in the cryostream, the heating by the X-ray beam is only a few degrees. This is not sufficient to raise the sample above the amorphous-ice/crystalline-ice transition temperature and, if the cryostream cools the sample to 100 K, not even enough to significantly enhance radiation damage from secondary effects.

**Keywords:** X-ray beam heating; thermal imaging; cryocooling; crystal; glass.

## 1. Introduction

With the advent of intense third-generation synchrotron sources, radiation damage to cryocooled macromolecular crystals can be a significant and undesirable feature of the experiment (Garman & Nave, 2002; Garman & Owen, 2006). Radiation damage can lead to errors in the interpretation of the resulting structure (Burmeister, 2000; Weik *et al.*, 2000; Grabolle *et al.*, 2006; Yano *et al.*, 2005; Dubnovitsky *et al.*, 2005). Cryocooling (Garman & Schneider, 1997; Hope, 1988; Rodgers, 1994, 1997; Garman, 1999) largely eliminates damage in the case of the laboratory source but is not completely successful at the synchrotron (Gonzalez & Nave, 1994; Gonzalez *et al.*, 1992). The X-ray beam not only causes radiation damage but also heats the sample. With a third-generation synchrotron source, the power and power density of the X-ray beam on the sample are great enough to raise concern over this heating. Radiation damage studies have shown both dose-rate-dependent (Leiros *et al.*, 2001, 2006; Ravelli *et al.*, 2002) and dose-rate-independent X-ray damage (Sliz *et al.*, 2003). The dose-rate-dependent damage has been

attributed to possible heating effects of the beam. At its most extreme, beam heating could conceivably warm the crystal above the amorphous-ice/crystalline-ice transition temperature which has been determined to be ~130–140 K (Johari *et al.*, 1987; McMillan & Loss, 1965). Theoretical models of sample heating by the beam have been proposed in the literature. Initially Helliwell developed an adiabatic model (Helliwell, 1984). Later models included convection and other refinements such as three-dimensional heat conduction and different sample shapes to increase fidelity (Mhaisekar *et al.*, 2005; Nicholson *et al.*, 2001; Kuzay *et al.*, 2001; Kriminski *et al.*, 2003; Helliwell, 1992; Kazmierczak *et al.*, 2007). However, experimental verification of the beam heating of the sample has not been previously achieved.

The rate of cryocooling has been investigated by thermocouple measurements (Walker *et al.*, 1998; Teng & Moffat, 1998). This technique has the disadvantage that the measured temperature may differ from that of the sample crystal due to the presence of the thermocouple and heat conduction along its wires. Non-invasive thermal imaging techniques obviate this concern. Initial thermal imaging studies were qualitative

# radiation damage

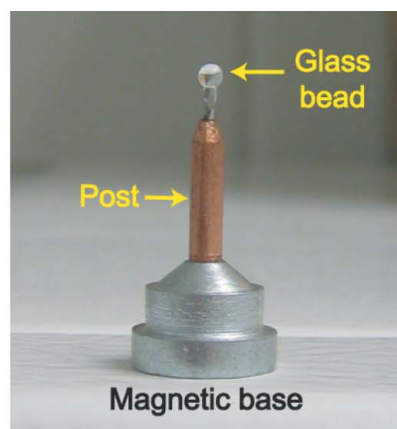
(Snell *et al.*, 2002, 2005) but experimental calibration has now allowed quantitative measurements of the sample temperature.

In this study, thermal imaging (Snell *et al.*, 2002) is used to optically image and measure sample heating by the beam. Ultimately, the data will allow verification of the computational models of beam heating (Kazmierczak *et al.*, 2007) so that the temperature in the sample can be accurately predicted and therefore used with confidence to help assess damage scenarios.

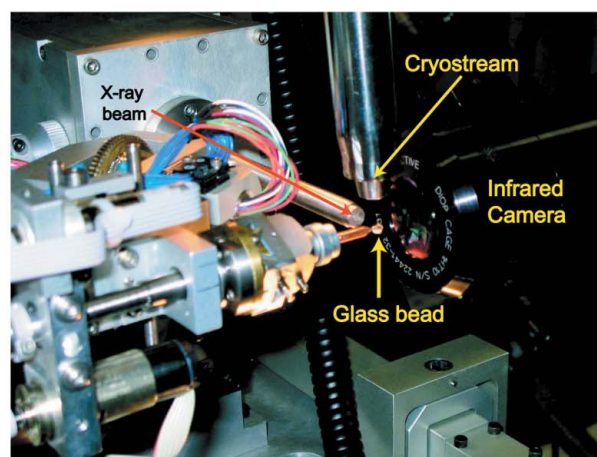
## 2. Experimental set-up and methodology

The aim of the experiment was to measure the temperature of a macromolecular crystal sample in an X-ray photon beam at 100 K. The infrared camera used has a sensitivity and accuracy proportional to temperature. As the temperature decreases, the power density of the infrared radiation emitted from the sample decreases (Snell *et al.*, 2002). The signal from the sample rapidly approaches the electronic noise in the system at a temperature which depends on the emissivity of the sample. For both protein crystals and glass the minimum useful temperature is inconveniently above the amorphous-ice/crystalline-ice transition point of  $\sim 130\text{--}140\text{ K}$  (Johari *et al.*, 1987; McMillan & Loss, 1965). The plan was to first measure the temperature rise with glass beads as models and then proceed to a biological crystal sample of about 0.2 mm in size. This would allow validation of recent model calculations for X-ray heating on a sphere of diameter 0.2 mm having X-ray properties of a protein crystal (Mhaisekar *et al.*, 2005). The selection of the photon energy to be used for the experiment was defined by the aim of maximizing the power absorbed in the small biological sample. The glass beads would fully absorb the beam power at the photon energy of 12.4–12.7 keV used most for macromolecular crystallography, but the 0.2 mm biological sample would only absorb 6% of the beam power. The product of undulator power and absorption coefficient was calculated. The maximum at 6.5 keV was selected as the appropriate photon energy for the whole experiment. However, after completing the measurements with the beads, the first trial with xylose isomerase crystals showed a rapid visible color change on irradiation. After illumination the sample had changed, adding an unnecessary complication to the temperature calibration described later. Thus, the experiment was, unfortunately, limited to the simplified ‘model’ system to validate theoretical treatments of beam heating. There was no reason to change the beamline to the ‘crystallographic’ photon energy of 12.4 keV and repeat the measurements with the bead since the absorbed beam power would have been only marginally higher.

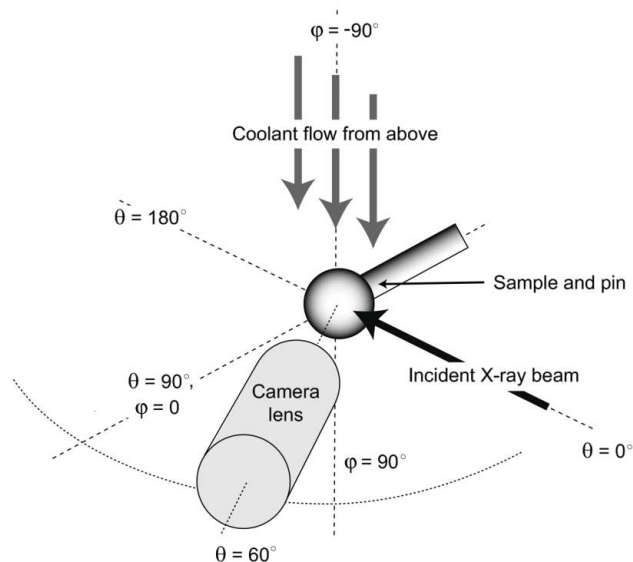
Samples were glass beads of diameter 1 mm and 2 mm (Walter Stern, Port Washington, NY, USA). The beads were mounted by epoxy directly to a standard Hampton Research cryo-pin (Fig. 1a). The X-ray absorption, and the other material properties of glass, are well characterized and listed in Tables 1 and 2. The absorption length at 6.5 keV was calculated from the composition and density data supplied by



(a)



(b)



(c)

**Figure 1**

Experimental set-up showing (a) the glass bead and mount used, (b) the bead and camera positioned on the beamline, and (c) a schematic of the coordinate system used. Note that in (b) the photograph shows the initial set-up, not the case used for measurements, where the camera is offset to look toward the front of the glass bead as shown in (c).

**Table 1**

Chemical composition of the glass bead surrogate crystal samples.

Chemical	% by weight
SiO <sub>2</sub>	66.0
B <sub>2</sub> O <sub>3</sub>	3.0
ZnO	2.0
K <sub>2</sub> O	1.0
Al <sub>2</sub> O <sub>3</sub>	5.0
CaO	7.0
MgO	1.0
Na <sub>2</sub> O	15.0

**Table 2**Physical parameters for the experimental system: glass data at 290 K from manufacturer, other data at 290 K from NIST and the available literature where appropriate (Lide, 2007; Marquardt *et al.*, 2001; Lemmon *et al.*, 2005).

	Glass bead	Stainless steel pin	Nitrogen
Density (g cm <sup>-3</sup> )	2.5	7.9	0.00118
Specific heat capacity (J kg <sup>-1</sup> K <sup>-1</sup> )	799	470	1015
Thermal conductivity (W m <sup>-1</sup> K <sup>-1</sup> )	0.97	15	0.025
Calculated X-ray attenuation length at 6.5 keV (mm)	0.051	–	631
Viscosity (kg m <sup>-1</sup> s <sup>-1</sup> )	–	–	1.74 × 10 <sup>-5</sup>

the manufacturer, and from tabulated absorption data (Henke *et al.*, 1993). The glass beads have the advantage of being spherical which makes a mathematical treatment easier than for a standard crystal sample, and the beads can be repeatedly warmed and cooled without damage.

Preliminary experiments with glass beads were carried out on the South East Regional CAT (SER-CAT) at the Advanced Photon Source (APS) at Argonne National Laboratory in order to establish an optimal experimental configuration and technique. The data collection described in this paper was subsequently carried out on the Structural Biology Center (SBC) undulator beamline (19-ID), also at the APS. An Indigo Systems Phoenix thermal imaging camera, described elsewhere (Snell *et al.*, 2002, 2005), was used with a 4× magnification lens to image the sample and non-intrusively measure its temperature. The sample was convectively cooled using an Oxford Cryosystems 700 Cryostream system. The experimental set-up is illustrated in Fig. 1(b). The optical axis of the camera is in the horizontal plane looking at the sample in the direction of the beam but rotated 60° away from the beam. The sample is mounted on the  $\varphi$  spindle of a  $\kappa$  goniostat at zero  $\kappa$  angle (spindle axis horizontal). The cold nitrogen gas stream has been moved to a vertical flow orientation to make room for the camera lens.

The beam size was measured as 0.103 mm FWHM horizontal (0.187 mm full width at tenth-maximum) and 0.084 mm FWHM vertical (0.153 mm full width at tenth-maximum). The beam size was not limited by slits. The synchrotron operated in top-up mode with the ring current at 102.7 mA during the ion chamber measurement and ranging between 101 and 103 mA during the experimental data collection. The beam intensity was measured by an ion chamber at the sample position at the start of the experiment. The photon flux ( $3.24 \times 10^{12}$  photons

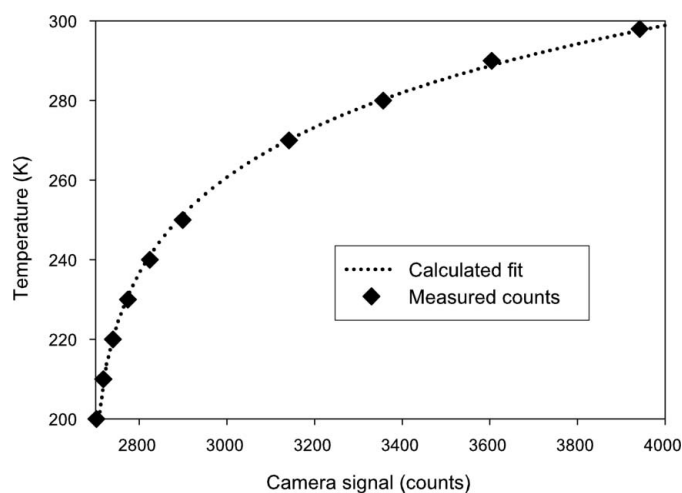
s<sup>-1</sup> ± 15%, photon energy 6.5 keV, beam power 3.37 mW) was calculated from the ion chamber current using 32 eV/electron-ion pair data (McMaster *et al.*, 1969) under standard conditions. A measured transmission filter had been inserted to prevent saturation of the ion chamber.

For the 2.0 mm glass bead experiments the cryostream was initially set to 100 K and an image taken of the bead before the shutter was opened (lowest calibration temperature). A set of sequential images was then recorded as the X-ray shutter was opened (transient heating experiments). Finally a single image was taken with the shutter open when the bead had reached steady state (temperature measurements at steady state). All the images were taken with 1 ms exposure time with the sequential set of images recorded at a frame repetition rate of 60 Hz. The same protocol was repeated with the cryostream temperature settings increased in 20 K increments up to 200 K and then with 10 K increments up to 290 K. At 290 K an additional experiment was carried out with the cryostream gas flow rate doubled to check for flow-dependent changes. The cryostream was then switched off and the bead allowed to warm to ambient temperature, 298 K, to obtain the final thermal image for the calibration curve (highest temperature used in calibration curve). The 2.0 mm bead was then replaced with a 1.0 mm bead and the experiments repeated. Since the diameter of the beads is larger than the dimensions of the beam and more than ten times the attenuation length (Table 2), both beads will absorb the full beam power.

The infrared camera provides an integrated intensity reading of the 3–5 μm radiation for each pixel. A calibration curve was established for converting the infrared camera pixel values into temperature values using images of the bead with the X-ray shutter closed and with the Cryostream at a known temperature. The calibration curve (Fig. 2) has the form

$$T = a(I - b)^c, \quad (1)$$

where  $T$  is the temperature in K,  $I$  is the intensity and  $a$ ,  $b$  and  $c$  are constants. For the 2 mm-diameter glass sphere case, the constants  $a$ ,  $b$  and  $c$  in (1) are 150.6, 2686 and 0.09547,

**Figure 2**

Calibration curve for the intensity versus temperature relation for the thermal imaging camera.

# radiation damage

respectively. For the 1 mm case,  $a$ ,  $b$  and  $c$  vary only slightly from the values above, and are 138.4, 2601 and 0.1062, respectively. The variation in the values of the constants is due to the empirical nature of the calibration curve. It should be noted that the gas temperature was taken to be the programmed ‘set point’ temperature of the Cryostream controller and that the actual temperature at the sample location may be slightly different. Measurements using a calibrated thermocouple at the sample position showed a maximum error of  $\pm 1.3$  K for set-point temperatures between 290 K and 250 K. The recorded images were processed using *Talon* (Indigo Systems, Santa Barbara, CA, USA) to produce ASCII pixel maps containing raw count measurements and then a *Matlab* (The Mathworks, Natick, MA, USA) program was used to convert them into temperature pixel maps using the above calibration equation.

As can be seen from the calibration curve, the useful range of temperature measurements for glass bead samples extends only down to about 200 K owing to the low emissivity of glass in the infrared at that temperature. Below this temperature the signal of the infrared camera is close to the electronic noise and, even for relatively large temperature changes of 10 K, the error in the measurement becomes significant. Hence for greatest sensitivity and least error, the data recorded at 290 K are presented in this analysis. The temperature difference between sample surface and gas is inversely proportional to the heat transfer coefficient  $h$  (for the same rate of heat flow). Since  $h$  changes only by about 5% for  $N_2$  between 100 K and 300 K [using equation (3) of Kriminski *et al.* (2003) for the dependence of  $h$  on thermal conductivity and dynamic viscosity of the gas and values for  $N_2$  in Table 1], data measured at 290 K are applicable to lower temperatures.

### 3. Results

The temperature increase during intense X-ray beam heating of spherical glass bead samples has been measured. Fig. 3 shows the temperature profile of the beam along its axis through the bead. The peak temperature rise in the 1 mm case (Fig. 3a) is 21.3 K where the beam is incident and the cooling gas stream is flowing at its normal rate,  $0.4 \text{ m s}^{-1}$ . When the gas stream flow rate is increased to turbo mode,  $0.8 \text{ m s}^{-1}$ , the peak temperature rise is reduced slightly to 19.9 K. In the 2 mm bead case (Fig. 3b) the maximum temperature rise is 10.9 K at normal gas flow rate decreasing to 9.9 K at double flow rate. In each case doubling the flow rate reduces the temperature by about 1 K over the entire observed surface of the bead. Measurements at lower gas stream temperatures (280–220 K) show an average peak temperature rise of  $\sim 23$  K with a standard deviation of 0.9 K and of  $\sim 10$  K with a standard deviation of 0.7 K for the 1 mm and 2 mm beads, respectively, confirming that temperature rise owing to the incident X-ray beam is essentially independent of the starting temperature.

Fig. 4 shows the spatial distribution of the temperature over the surface of the glass beads with the gas stream at normal

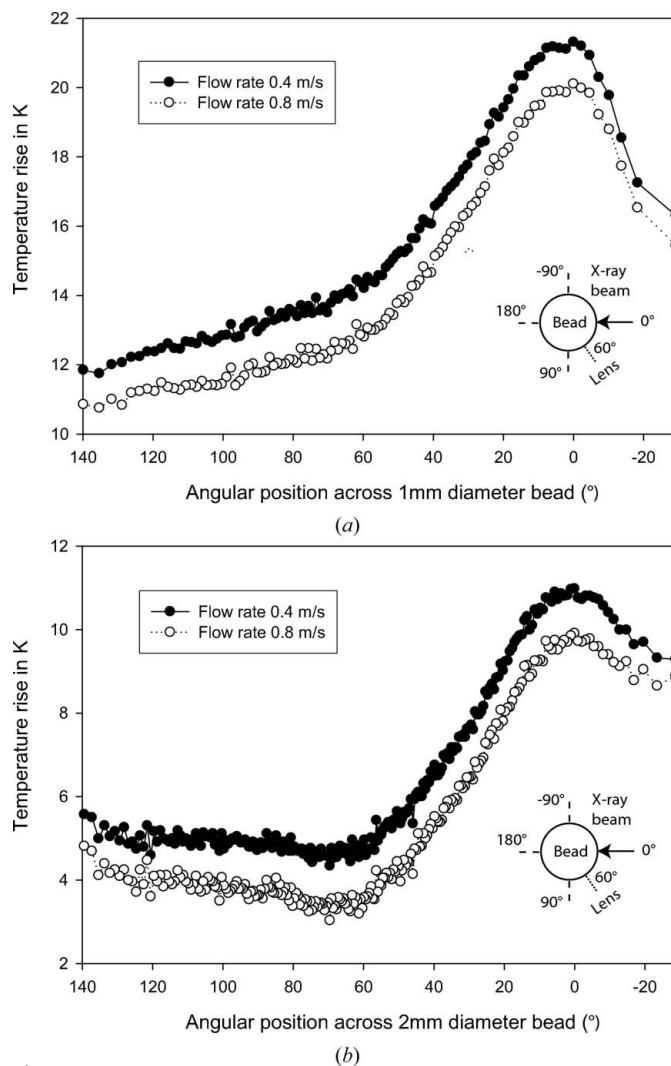


**Figure 3** Temperature plotted across horizontal axis of (a) the 1 mm and (b) the 2 mm glass bead. The gas stream was at 290 K and the vertical axis shows temperature relative to the gas stream temperature. The angular position is defined in Fig. 1(c).

flow at 290 K and the shutter open. The figure is false-colored such that red is hot and blue is cold. Each bead is plotted on a separate absolute temperature scale to show both the heating effect of the incident beam and the cooling effect of the cryostream incident from the top of the figure. Small imperfections in the sensor are seen in both images but do not affect the measured data. The beam does not hit the exact center of the bead owing to minor positioning error.

In addition to spatial information, infrared imaging also provides temporal information. Fig. 5 shows the temperature rise on the beads after the shutter is opened. The temperature is measured where the beam hits the bead, averaged over the beam area, and also as an average of the whole observed surface of the bead. For both beads the temperature rise has been measured with the gas stream flowing at 290 K and with the gas stream blocked. In the 1 mm bead case, without gas flow, the whole bead is still warming after 5 s of illumination. With the cold nitrogen gas flowing the temperature rise starts

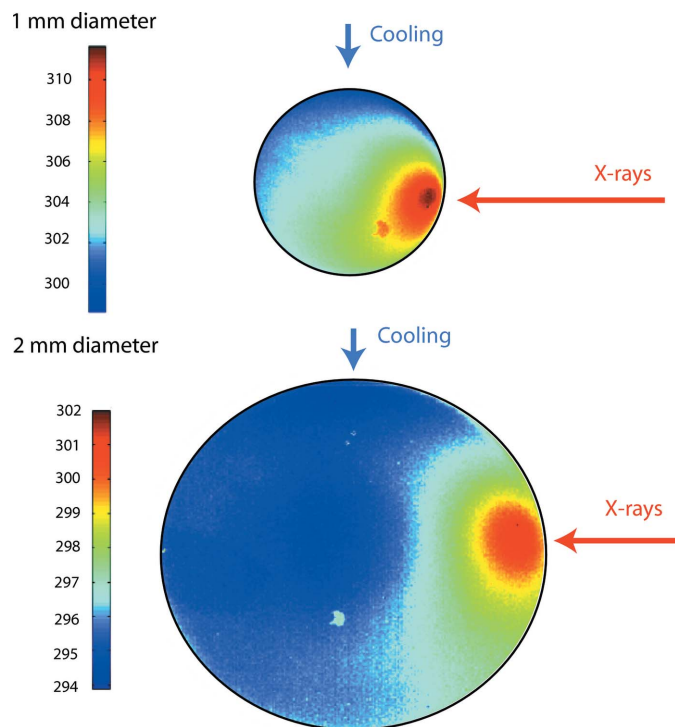


**Figure 4** False-color images of the 1 mm and 2 mm glass beads with the synchrotron beam incident on them. Images were generated from the data reported here using *Matlab* and provided by Dr Michael Kazmierczak. Cooling is from the top with the X-ray beam incident on the right-hand side.

to slow at about 4 s. For the 2 mm case the bead is still heating after 5 s for both cases.

The pronounced temperature peaks at the locations where the beam strikes in Fig. 3 are due to the small attenuation length of the glass; 80% of the beam power is absorbed within a depth of 0.083 mm (within a volume of  $\sim 0.1 \text{ mm} \times 0.08 \text{ mm} \times 0.08 \text{ mm}$ ). These peaks would not occur if the attenuation length were much greater than the absorber size, as is the case for biological samples, since the heat deposition is then almost uniform along the beam path. Consequently, for extrapolation of the measured temperature rises of the beads to biological samples (see §4), the average bead temperature rises over 3 s are used (this is a typical exposure time at the APS; see below) (Fig. 5). They are  $\sim 14 \text{ K}$  for the 1 mm bead and  $\sim 4 \text{ K}$  for the 2 mm bead. The measured temperature rise between bead and gas is also meaningful for a biological sample because the heat transfer from surface to gas is dependent on the properties of the gas but not on the surface material.

#### 4. Discussion and conclusions

In imaging beam heating on glass beads, significant temperature rises are seen. The glass beads are simple to geometrically model and chemically well characterized. The heating is not sufficient to raise the sample temperature to the amorphous/crystalline ice transition region,  $\sim 130\text{--}140 \text{ K}$  (Johari *et al.*, 1987; McMillan & Loss, 1965), under typical conditions, *i.e.* the gas stream operating at 100 K. How suitable is the glass bead

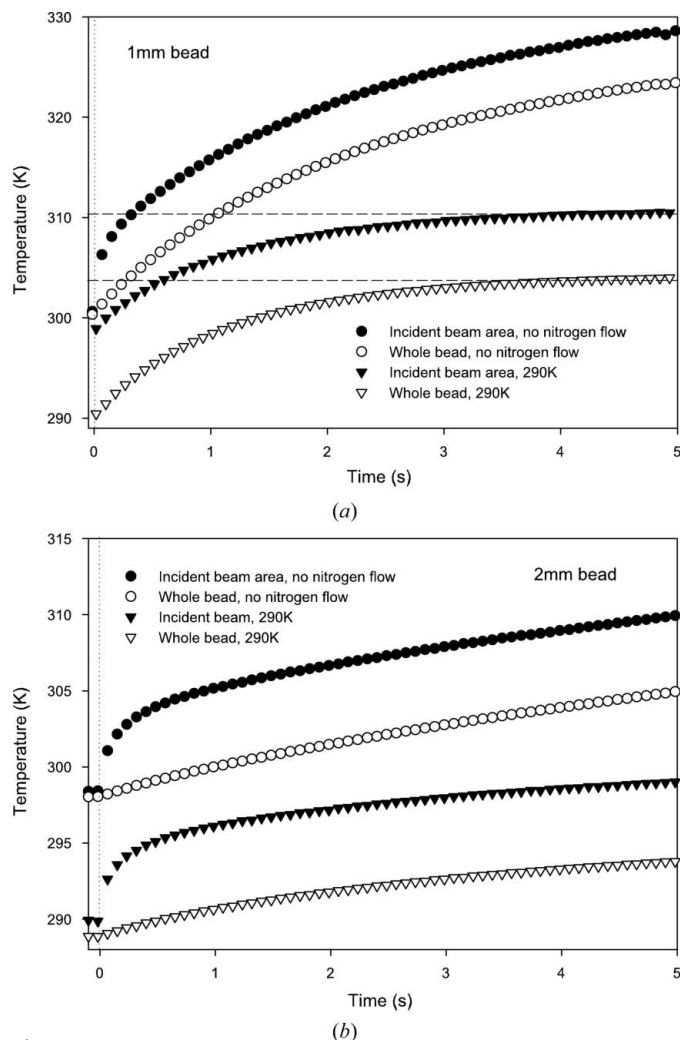


**Figure 5** Plot of the temperature for (a) the 1 mm and (b) the 2 mm beads, at the point where the beam hits the bead and averaged over the whole bead with no nitrogen flow and flow at 290 K. Time zero is the point when the shutter opens. Only every fifth data point is plotted for clarity.

as a model to represent a macromolecular crystal? Is beam heating significant for macromolecular crystals, which of course are not glass beads? For a typical protein sample (taken from examples of sequence statistics in the Bioinformatics toolbox of *Matlab*, 50% solvent content, density  $1.17 \text{ g cm}^{-3}$  at room temperature,  $\sim 1.25 \text{ g cm}^{-3}$  at 100 K based on average partial specific volume of protein in crystal of  $0.74 \text{ cm}^3 \text{ g}^{-1}$ ), the absorption length is about 0.477 mm at 6.5 keV, and about 3.406 mm and 3.621 mm at photon energies of 12.4 keV ( $1 \text{ \AA}$ ) and of the Se *K*-edge (12.66 keV), respectively (exemplary sample containing no selenium), which are most frequently used for macromolecular crystallography [calculated using data from Henke *et al.* (1993)].

In the following the measured temperature rise of the beads is extrapolated to representative data-collection conditions at third-generation sources and the temperature rise of typical samples is predicted. Published model calculations are used as a guide for scaling the temperature rise with sample size and absorbed power. The model calculations are validated by

**Table 3**

Data on the physical properties of nitrogen, amorphous ice and a protein crystal at 100 K taken from available literature (Lide, 2007; Lemmon *et al.*, 2005; Kriminski *et al.*, 2003).

	Nitrogen	Amorphous ice	Protein crystal
Density (g cm <sup>-3</sup> )	0.00348	0.93	1.25
Specific heat capacity (J kg <sup>-1</sup> K <sup>-1</sup> )	1015	830	600
Thermal conductivity (W m <sup>-1</sup> K <sup>-1</sup> )	0.010	7	5
Calculated X-ray attenuation length at 12.4 keV (mm)	1556	4.075	3.406
Viscosity (kg m <sup>-1</sup> s <sup>-1</sup> )	$6.96 \times 10^{-6}$	–	–

scaling the models to the size and absorbed power of the beads. The temperature rise has two components, the internal temperature gradient between where the beam deposits energy and the surface of the sample, and the external temperature drop between the surface and the cooling gas. The difference between average temperature rise and the peak, observed on the beads at the location where the beam hits, could be used to separate the internal and external components. However, this peak is a special case, owing to the short attenuation length of glass. It does not occur in samples with an attenuation length much greater than the sample size, such as biological samples or the samples in the model calculations. Extrapolation of the internal component would not be meaningful. Therefore, the internal component is derived from the model calculations using conservative estimates of thermal conductivity. For extrapolating the external component, the average bead temperature rise is used as a starting point. This is justified as a very large fraction of the surface is at the average temperature (Fig. 4).

A survey at several macromolecular crystallography beamlines at the APS yields the following parameters for X-ray data collection: average crystal sizes, 0.02–0.10 mm, typically 0.05 mm; loop sizes, 0.02–0.20 mm, typically 0.10 mm; beam sizes on the sample, 0.02–0.15 mm square, typically 0.08 mm square; photon energy, almost always 12.4 keV (1 Å) or 12.658 keV; fluxes,  $1.0\text{--}2.5 \times 10^{12}$  photons s<sup>-1</sup>, typically  $1.5 \times 10^{12}$  photons s<sup>-1</sup>; exposure time per frame, 0.5–3 s, typically 3 s. Using the typical parameters and the attenuation length from Table 3, the power absorbed by the typical sample (crystal and ice in the loop) is 0.087 mW, about 1/40 of the power absorbed by the beads. The small sample size, comparatively large attenuation length (resulting in uniform heat deposition along the beam path) and the very short distances to the surface combine to create a very small temperature gradient  $\Delta T_{\text{int}}$  within the sample. This has been calculated for a simple model of a circular disc perpendicular to the beam by Rosenbaum & Kazmierczak (2002) as  $\Delta T_{\text{int}} = 0.019$  K (0.006 K from the beam center to the perimeter of the beam and 0.013 K from there to the perimeter of the disc) for  $1 \times 10^{12}$  photons s<sup>-1</sup> of 12 keV in a 0.1 mm × 0.1 mm beam, 0.3 mm loop diameter and thermal conductivity coefficient  $k = 5$  W m<sup>-1</sup> K<sup>-1</sup> (Table 3). A more refined estimate by Kriminski *et al.* (2003) gives  $\Delta T_{\text{int}} = (1\text{--}8) \times 10^{-3}$  K for  $2 \times 10^{11}$  photons s<sup>-1</sup> of 13 keV onto a 0.2 mm-diameter sphere for  $k$  in the range 0.6–5 W m<sup>-1</sup> K<sup>-1</sup>. A newer estimate by Mhaisekar *et al.* (2005) arrives at  $\Delta T_{\text{int}} = 0.556$  K, 0.543 K and 0.560 K for  $3 \times 10^{12}$  photons s<sup>-1</sup> of 13 keV in a 0.1 mm-diameter beam onto spheres of diameter 0.2 mm, 0.4 mm and 0.8 mm, respectively, using a more conservative value of 0.6 W m<sup>-1</sup> K<sup>-1</sup> for the thermal conductivity. The internal temperature rise for the ‘typical’ sample can then be safely estimated to be less than 0.25 K using a conservatively low thermal conductivity.

For the external temperature rise between the sample surface and gas,  $\Delta T_{\text{ext}}$ , the model samples are first scaled to the 1 mm-diameter glass bead to validate the model, then the model calculations are scaled down to 0.1 mm size samples. Kriminski *et al.* (2003) derived  $\Delta T_{\text{ext}} \simeq L^{-1/2}$  for a sphere of diameter  $L$  for the same incident flux [equation (15) in that reference, after multiplying the flux density with the cross section of the sphere]. Mhaisekar *et al.* (2005) calculated numerical solutions for spheres of 0.8 mm, 0.4 mm and 0.2 mm with the same flux in a 0.1 mm-diameter beam (Table 8 from this reference) and found a very small increase in  $\Delta T_{\text{ext}}$  from 5.88 K to 6.06 K and to 7.16 K, respectively, or  $\Delta T_{\text{ext}} \simeq L^{-0.14}$ . In order to make comparisons with the measured temperature rises for the beads which both absorb the full beam, the temperature rises are multiplied by  $L^{-1}$  to adjust to constant absorbed power. Then Kriminski *et al.* (2003) predicted  $\Delta T_{\text{ext}} \simeq L^{-3/2}$ , and Mhaisekar *et al.* (2005) predicted  $\Delta T_{\text{ext}} \simeq L^{-1.14}$ . Scaling Mhaisekar’s 0.8 mm sphere data up to 1 mm using  $L^{-1.14}$  and linear scaling for absorbed power from 1.21 mW in the model to 3.37 mW for the bead, Mhaisekar’s model predicted  $\Delta T_{\text{ext}} = 12.7$  K for the 1 mm bead. The measured average temperature rise for the 1 mm bead is  $\sim 14$  K. The agreement between model and measurement appears to be good enough to justify extrapolating from Mhaisekar’s 0.2 mm sphere model down to the ‘typical’ 0.1 mm-size biocrystal sample. Using the above scaling for size and absorbed power,  $\Delta T_{\text{ext}} = 7.2$  K for Mhaisekar’s 0.2 mm sphere model absorbing 0.31 mW is extrapolated to  $\Delta T_{\text{ext}} = 4.5$  K for the ‘typical’ 0.1 mm sample absorbing 0.087 mW. Adding the internal temperature rise of less than 0.25 K, the maximum realistic temperature increase inside the crystal sample is then, based on the glass bead measurements and model calculations, less than 5 K. Because of the wide variability of data-collection parameters stated above, the temperature rise in any particular case may range from 0.2 to 2 times the rise extrapolated for the typical case.

Calculations based on the experimental measurements show that beam heating should not be a significant problem with regard to devitrification of cryoprotected samples for typical loop sizes, fluxes and photon energies currently used for macromolecular crystallography data collection at third-generation sources. Free radicals become mobile at a temperature of 120–130 K (Becker *et al.*, 1994; Sevilla *et al.*, 1991); above 120 K, manifestation or expression of radiation damage may be enhanced. The model calculations by Mhaisekar *et al.* (2005) quoted above show that for the same flux intercepted by the sample the temperature rise increases very little with decreasing sample diameter (about 20% for a fourfold decrease in diameter). So, under normal conditions of

data collection in a 100 K gas stream there appears to be a fairly wide margin for avoiding detrimental crystal heating even with respect to enhanced free-radical propagation.

However, microcrystals require more careful considerations. The integrated intensity of the diffraction peaks is proportional to the product of flux intercepted by the crystal, crystal thickness and exposure time per frame. If the experimenter chooses to increase the flux on the sample instead of increasing the exposure time to make up for the smaller sample thickness in order to achieve the same intensity of the recorded diffraction peaks, they may steer into dangerous territory. The same caveat applies to radiation damage studies where maximum fluxes are used instead of just maximum flux densities. A flux of  $6 \times 10^{12}$  photons  $s^{-1}$  intercepted by the sample, *i.e.* four times the 'typical' flux used for the extrapolation, would result in a predicted temperature rise of 20 K ( $\sim 24$  K for a 0.025 mm-diameter sample). This, indeed, would bring the sample close to the onset of enhanced free-radical mobility with associated consequences for radiation damage.

All data were collected at the APS, preliminary data at the SER-CAT beamlines, 22-ID and 22-BM. The data presented in this paper were collected at the SBC beamline, 19-ID. We thank Dr Michael Kazmierczak who suggested the use of glass beads as sample surrogates and provided them. We also thank Drs Norma Duke, Steve Ginell and Frank Rotella at the Structural Biology Center for assistance during data collection, Dr Bill Bernhard at the University of Rochester, and the referees for useful comments. Use of the Advanced Photon Source was supported by the US Department of Energy, Office of Science, Office of Basic Energy Sciences, under Contract No. W-31-109-Eng-38. EHS and MDW were supported by NASA grant NAG8-1928. EHS is grateful to the John R. Oishei Foundation for their generous support. HDB is partially supported by the Louisiana Governor's Biotechnology Initiative.

## References

- Becker, D., Lavere, T. & Sevilla, M. D. (1994). *Radiat. Res.* **140**, 123–129.
- Burmeister, W. P. (2000). *Acta Cryst.* **D56**, 328–341.
- Dubnovitsky, A. P., Ravelli, R. B. G., Popov, A. N. & Papageorgiou, A. C. (2005). *Protein Sci.* **14**, 1498–1507.
- Garman, E. (1999). *Acta Cryst.* **D55**, 1641–1653.
- Garman, E. & Nave, C. (2002). *J. Synchrotron Rad.* **9**, 327–328.
- Garman, E. F. & Owen, R. L. (2006). *Acta Cryst.* **D62**, 32–47.
- Garman, E. F. & Schneider, T. R. (1997). *J. Appl. Cryst.* **30**, 211–237.
- Gonzalez, A. & Nave, C. (1994). *Acta Cryst.* **D50**, 874–877.
- Gonzalez, A., Thompson, A. W. & Nave, C. (1992). *Rev. Sci. Instrum.* **63**, 1177–1180.
- Grabolle, M., Haumann, M., Muller, C., Liebisch, P. & Dau, H. (2006). *J. Biol. Chem.* **281**, 4580–4588.
- Helliwell, J. R. (1984). *Rep. Prog. Phys.* **47**, 1403–1497.
- Helliwell, J. R. (1992). *Macromolecular Crystallography with Synchrotron Radiation*. Cambridge University Press.
- Henke, B. L., Gullikson, E. M. & Davies, J. C. (1993). *Atom. Data Nucl. Data Tables*, **54**, 181–342.
- Hope, H. (1988). *Acta Cryst.* **B44**, 22–26.
- Johari, G. P., Hallbrucker, A. & Mayer, E. (1987). *Nature (London)*, **330**, 552–553.
- Kazmierczak, M., Kumar, R., Gopalakrishnan, P. & Banerjee, R. (2007). In preparation.
- Kriminski, S., Kazmierczak, M. & Thorne, R. E. (2003). *Acta Cryst.* **D59**, 697–708.
- Kuzay, T. M., Kazmierczak, M. & Hsieh, B. J. (2001). *Acta Cryst.* **D57**, 69–81.
- Leiros, H.-K. S., McSweeney, S. M. & Smalas, A. O. (2001). *Acta Cryst.* **D57**, 488–497.
- Leiros, H. K., Timmins, J., Ravelli, R. B. & McSweeney, S. M. (2006). *Acta Cryst.* **D62**, 125–132.
- Lemmon, E. W., McLinden, M. O. & Friend, D. G. (2005). *NIST Chemistry WebBook, NIST Standard Reference Database Number 69*, edited by P. J. Linstrom and W. G. Mallard. Gaithersburg, MD: National Institute of Standards and Technology.
- Lide, D. R. (2007). Editor. *CRC Handbook of Chemistry and Physics*, 87th ed. Boca Raton, FL: Taylor and Francis.
- McMaster, W. H., Del Grande, N. K., Mallett, J. H. & Hubbel, J. H. (1969). Report UCRL-50174, Sec II, Rev. 1. Lawrence Livermore National Laboratory, USA.
- McMillan, J. A. & Loss, S. C. (1965). *Nature (London)*, **206**, 806–807.
- Marquardt, E. D., Le, J. P. & Radebaugh, R. (2001). *11th International Cryocooler Conference*, edited by R. G. J. Ross. Keystone, CO: Kluwer; New York: Plenum.
- Mhaisekar, A., Kazmierczak, M. J. & Banerjee, R. (2005). *J. Synchrotron Rad.* **12**, 318–328.
- Nicholson, J., Nave, C., Fayz, K., Fell, B. & Garman, E. (2001). *Nucl. Instrum. Methods*, **487**, 1380–1383.
- Ravelli, R. B., Theveneau, P., McSweeney, S. & Caffrey, M. (2002). *J. Synchrotron Rad.* **9**, 355–360.
- Rodgers, D. W. (1994). *Structure*, **2**, 1135–1140.
- Rodgers, D. W. (1997). *Methods in Enzymology*, Vol. 276, *Macromolecular Crystallography Part B*, edited by C. W. J. Carter and R. M. Sweet, pp. 183–203. New York: Academic Press.
- Rosenbaum, G. & Kazmierczak, M. (2002). *Acta Cryst.* **A58**(Suppl.), C279.
- Sevilla, M. D., Becker, D., Yan, M. Y. & Summerfield, S. R. (1991). *J. Phys. Chem.* **95**, 3409–3415.
- Sliz, P., Harrison, S. C. & Rosenbaum, G. (2003). *Structure*, **11**, 13–19.
- Snell, E. H., Judge, R. A., Larson, M. & van der Woerd, M. J. (2002). *J. Synchrotron Rad.* **9**, 361–367.
- Snell, E. H., van der Woerd, M. J., Miller, M. D. & Deacon, A. M. (2005). *J. Appl. Cryst.* **38**, 69–77.
- Teng, T. Y. & Moffat, K. (1998). *J. Appl. Cryst.* **31**, 252–257.
- Walker, L. J., Moreno, P. O. & Hope, H. (1998). *J. Appl. Cryst.* **31**, 954–956.
- Weik, M., Ravelli, R. B. G., Kryger, G., McSweeney, S., Raves, M. L., Harel, M., Gros, P., Silman, I., Kroon, J. & Sussman, J. L. (2000). *Proc. Natl. Acad. Sci. USA*, **97**, 623–628.
- Yano, J., Kern, J., Irrgang, K. D., Latimer, M. J., Bergmann, U., Glatzel, P., Pushkar, Y., Biesiadka, J., Loll, B., Sauer, K., Messinger, J., Zouni, A. & Yachandra, V. K. (2005). *Proc. Natl. Acad. Sci. USA*, **102**, 12047–12052.